



An adaptive Newton multigrid method for a model of marine ice sheets



Guillaume Jovet^{a,*,1}, Carsten Gräser^{a,b}

^a Department of Mathematics and Computer Science, Freie Universität Berlin, Berlin, Germany

^b DFG Research Center Matheon, Berlin, Germany

ARTICLE INFO

Article history:

Received 5 December 2012

Received in revised form 26 May 2013

Accepted 25 June 2013

Available online 4 July 2013

Keywords:

Marine ice sheets

Grounding line

p -Laplace

Newton multigrid method

Adaptive method

ABSTRACT

In this paper, we consider a model for the time evolution of three-dimensional marine ice sheets. This model combines the Shallow Ice Approximation (SIA) for the ice deformation, the Shallow Shelf Approximation (SSA) for the basal sliding, and the mass conservation principle. At each time step, we solve a scalar p -Laplace minimization-type problem with obstacle (SIA), a vectorial p -Laplace minimization-type problem (SSA) and a transport equation (mass conservation). The two minimization problems are solved using a truncated nonsmooth Newton multigrid method while the transport equation is solved using a vertex-centred finite volume method. Our approach is combined to an heuristic mesh adaptive refinement procedure to face the large gradients of the solution that are expected between the ice sheet and the ice shelf. As applications, we present some simulations of the Marine Ice Sheet Model Intercomparison Project MISIP (2D and 3D) and validate our results against an analytic solution (2D) and other participant model results (3D). Further numerical results show that the convergence of our Newton multigrid method is insensitive to local refinements making our overall adaptive strategy fully efficient.

© 2013 Elsevier Inc. All rights reserved.

1. Introduction

Warming in recent decades has caused a number of worldwide ice sheets to shrink substantially. As an example, the melting of Antarctic ice sheets has increased the global sea-level by ~ 0.4 mm per year during 2002–2005 [41]. Most of this mass loss came from the West Antarctic Ice Sheet (WAIS) [24]. The specificity of the WAIS is that most of its bedrock is located below the sea-level. Currently, only around one fourth of the WAIS is floating. However, this ratio might increase if the layer of ice gets thinner. In such condition, the Grounding Line (GL), that separates the grounded ice sheet and the floating ice shelf, might retreat by hundreds of kilometers. Moreover, GLs are well known to control the stability of marine ice sheets since they are unstable over upward-sloping bed [37]. Therefore, only a small slimming of the ice sheet might cause the GL to move rapidly backward if there is a depression in the bedrock at the GL position. As a consequence, this would automatically enhance the subglacial melting and rise the sea-level [1].

The physics of ice sheets becomes more complex when substantial parts are floating over the sea such that the effects of water must be accounted for. Indeed, ice sheets move mainly by ice deformation while floating ice shelves move mainly by basal sliding [43]. In between, some narrow transition zones where both processes play significant roles exhibit sharp changes in ice velocity profiles from shear-dominant to sliding-dominant. The motion of ice is usually described by a non-linear Stokes equation, the ice being considered as an incompressible non-Newtonian fluid [21]. As a boundary condition,

* Corresponding author.

E-mail address: guillaume.jovet@fu-berlin.de (G. Jovet).

¹ Supported by the Deutsche Forschungsgemeinschaft (project KL 1806 5-1).

friction on the bedrock can be described by power-type, linear-type, or Coulomb laws [36] while perfect sliding occurs where ice is floating. In fact, only the vertical shear (resp. longitudinal) components of the stress tensor are significant in most of shallow ice sheets (resp. shelves) [43]. Simplified shallow ice models – that are mostly used by glaciologists – are derived from such observations. More precisely, simplifications occur by neglecting the terms where the small aspect ratio of ice sheets (in the order of 10^{-3}) appears in the dimensionless Stokes equations. As a result, the Shallow Ice Approximation (SIA) model [21] accounts only for the vertical shear. Similarly, the Shallow Shelf Approximation (SSA) model [36] accounts for the longitudinal stresses and the friction on the bedrock. In the last ten years, more or less simplified mechanical models have been involved in marine ice sheets models. Vertically-integrated models are the most popular ones since they are two-dimensional, which considerably reduces the size and the complexity of the system to solve. Among these models, those based on the SSA are the most common [9,15,32,37,42,29]. Some attempts to include the vertical shearing into two-dimensional (still vertically-integrated) models have been made by coupling the SIA to the SSA (independently) [43] or in a more sophisticated way using the Schoof–Hindmarsh model [8]. Finally, the most accurate models are three-dimensional like the First Order Approximation (FOA) [5,6,29] or the full Stokes model [10,29]. Let us notice that the SSA, the FOA and the Stokes models have been combined using a domain decomposition in [39].

Among the above contributions, one can distinguish two strategies for the numerical treatment of the GL. Since the grounded and floating domains evolve over time, one can follow the GL exactly or use an approximation. In both cases, the floating domain is determined by a geometrical criterion resulting from Archimedes principle. In the first case, a criterion determines how to move the mesh together with the GL [9,37]. Each domain (floating or grounded) involves a different model and a boundary condition imposes the continuity of stresses at the GL. Moving a one-dimensional mesh—that corresponds to a two-dimensional ice sheet—is an easy task since the GL is a single point. However, this becomes harder with one more horizontal dimension since the GL is a curve [34]. To overcome such difficulty, the second approach considers a unified model for the ice sheet and for the ice shelf with an implicit description of the GL through the flotation criterion. This criterion designs which points of the mesh are in the floating part and which points are in the grounded part such that different sliding conditions can be applied. Such an approach must be combined with an adaptive mesh refinement procedure to deal with the sharp changes in the ice flow regime that are expected close to GL [34]. The implementation of moving or adaptive meshes is strongly connected to the numerical method, which is used to solve the mechanical equations. Existing shallow ice sheet and ice shelf models are based on the three most popular numerical techniques: finite differences [9,32,42,43], finite volumes [8] and finite elements [15,10]. It is well known that these techniques do not offer the same flexibility in term of re-meshing. Indeed, finite differences usually require structured meshes. In contrast, finite element and finite volume techniques can deal more easily with locally refined and unstructured meshes.

In this paper, we implement an isothermal ice sheets and ice shelves model that is based on a linear superposition of the SIA model and of the SSA model. Such superposition assumes that the modeling of the horizontal and the vertical ice flows can be linearly decoupled. This assumption is physically justified for most ice sheets and ice shelves [43]. A weighted combination of these two models was originally proposed in [7] and later modified into a simple superposition in [43]. There are two ways of superposing SIA and SSA velocity components. The simplest way consists of summing both components such that the mass conservation equation remains a pure advection problem. The second approach, which is adopted in this paper, includes directly the explicit SIA component in the mass conservation, which acts as an additional nonlinear diffusion term due to the gradient involved in the SIA flux [25]. Diffusion and advection are decoupled by a first order splitting algorithm, such that it remains to solve at each time step two p -Laplace problems (one for the SSA and one for the SIA) and one transport equation. On one hand, both p -Laplace problems are approximate using the Truncated Nonsmooth Newton MultiGrid (TNMNG) method [17,18], which consists of a nonlinear relaxation scheme combined with Newton-type multigrid corrections. On the other hand, a vertex-centred finite volume method is advocated to solve the convection part of the model. Finally, we implement a heuristic adaptive local mesh refinement procedure to increase the accuracy close to GL.

Our model has been shortly presented in [26] for a non-realistic two-dimensional ice sheet, which writes as a one-dimensional mathematical problem. The goal of this paper is to extend the model to real three-dimensional marine ice sheets. Adding one horizontal dimension to the model obliges us to revise the meshing procedure. In particular, our solver relies on a geometrical multigrid approach, which requires regular, conform and – most importantly – hierarchical meshes. The construction of such one-dimensional adaptive meshes is straightforward. In contrast, further attention is required to not destroy the properties of a two-dimensional mesh such that efficiency of the geometrical multigrid method remains intact through the adaptive mesh refinement process. The reduction of computational costs by implementing an adaptive refinement procedure is another challenge of three-dimensional models. Finally, this paper dedicates a large part to applications and numerical results. In particular, we apply our method to the test problems proposed by the Marine Ice Sheet Model Intercomparison Project (MISMIP) in two and three dimensions [34,33]. This allows us to compare our results to the ones of the other participating models and the efficiency of our adaptive re-meshing strategy. In particular, we verify the ability of the adaptive mesh procedure to reproduce a reversible GL after being perturbed in the ice flow and sliding parameters. As an additional outcome, we point out a limitation of the superposed “SSA + SIA” model in describing the GL behaviour, which is a consequence of the uncoupling between the SSA and SIA velocity components. Finally, we provide some numerical results concerning the performance of our nonlinear multigrid solver in term of convergence and computational costs.

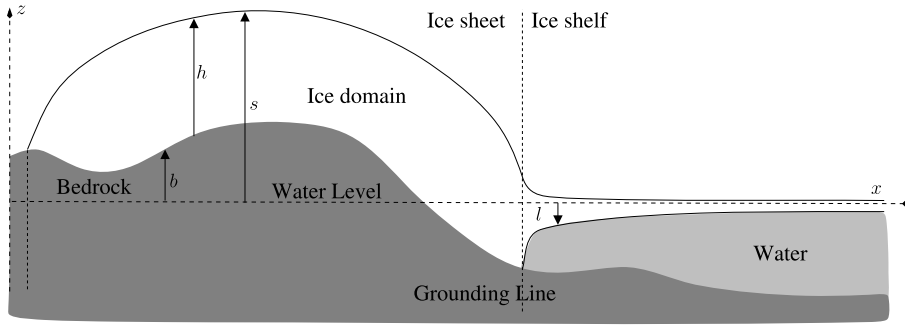


Fig. 1. Vertical section of a system ice sheet/shelf with notations.

The outline of this paper is the following. In Section 2, we formulate the superposed “SSA + SIA” model. Then, we describe the time and space approximation in Section 3. Finally, the numerical results are displayed in Section 4.

2. Model

In this paper we describe two- and three-dimensional ice sheet models starting with the latter. For the three-dimensional model ($d = 3$), the ice sheet extends over a two-dimensional horizontal domain contained in $\Omega \subset \mathbb{R}^2$. Its height and all other quantities will be described as functions over Ω . If we assume that the three-dimensional ice sheet is constant in one horizontal direction y , we can describe it on a single vertical section at $y = 0$, leading to a two-dimensional ice sheet model ($d = 2$), see Fig. 1. In this model the ice sheet extends over a one-dimensional horizontal domain contained in $\Omega \subset \mathbb{R}$ that is orthogonal to the direction y of constant shape. Although such ice sheet is not physical, it is useful for the sake of understanding.

In the following we assume that $\Omega \subset \mathbb{R}^{d-1}$ is an open convex set that represents the horizontal support of the ice sheet. The d -dimensional volume of grounded or floating ice is then contained in $\Omega \times \mathbb{R}$ and described by functions over Ω . We denote the horizontal coordinates by $\mathbf{x} \in \Omega$ with $\mathbf{x} = (x, y)$ for $d = 3$ and $\mathbf{x} = x$ for $d = 2$ and the vertical coordinate by z .

In this paper $\nabla = \nabla_{\mathbf{x}}$, $\nabla \cdot = \nabla_{\mathbf{x}} \cdot$ denote gradient and divergence, respectively, with respect to the horizontal variables \mathbf{x} . Let $[0, T]$ be a time interval, with $T > 0$. We suppose a fixed bedrock described by the elevation function $z = b(\mathbf{x})$ in Ω , and we denote by $l = l(\mathbf{x}, t)$ and $s(\mathbf{x}, t)$ the elevation of the lower and upper ice surfaces at time t and abscissa \mathbf{x} , respectively. Obviously, the inequality $b(\mathbf{x}) \leq l(\mathbf{x}, t) \leq s(\mathbf{x}, t)$ holds for all $\mathbf{x} \in \Omega$ and all $t \in [0, T]$, $b = l$ where ice is grounded, $l > b$ where ice is floating and $l = s$ outside the ice domain Ω , see Fig. 1. We denote by $h = s - l$ the ice thickness function.

2.1. Shelf flotation

The flotation of ice is driven by Archimedes principle. Call g the acceleration of gravity, ρ and ρ_w the densities of ice and water, respectively. At any point \mathbf{x} such that $h(\mathbf{x}) > 0$, if the buoyancy $-\rho_w g b(\mathbf{x})$ exceeds the force exerted by ice $\rho g h(\mathbf{x})$, then ice is floating, otherwise ice is grounded. Moreover, when ice is floating, the thickness of the rising part is $(1 - (\rho/\rho_w))$ of the total ice thickness. The application of Archimedes principle can be summarized by the relation

$$l = \max \left\{ b, -\frac{\rho}{\rho_w} h \right\}. \quad (1)$$

The set of points \mathbf{x} satisfying $b(\mathbf{x}) + \frac{\rho}{\rho_w} h(\mathbf{x}) = 0$ is the so-called Grounding Line (GL), which delimits the grounded and floating parts.

2.2. Velocity field

Following [7], the horizontal velocity field $\mathbf{u}_{TOT}(\mathbf{x}, z, t) \in \mathbb{R}^{d-1}$ of any ice particle in the ice domain $\{(\mathbf{x}, z) \in \Omega \times \mathbb{R}, l(\mathbf{x}) \leq z \leq s(\mathbf{x})\}$ is the sum of a constant in z component \mathbf{u}_{SSA} and a non-constant component \mathbf{u}_{SIA} [43]

$$\mathbf{u}_{TOT} = \mathbf{u}_{SIA} + \mathbf{u}_{SSA}. \quad (2)$$

Here, $\mathbf{u}_{SIA}(\mathbf{x}, z, t) \in \mathbb{R}^{d-1}$ is the horizontal velocity resulting from ice shearing which is described by the Shallow Ice Approximation (SIA), while $\mathbf{u}_{SSA}(\mathbf{x}, t) \in \mathbb{R}^{d-1}$ (also called \mathbf{u}) is the horizontal velocity induced by longitudinal stresses which is described by the Shallow Shelf Approximation (SSA). The SIA and the SSA models are described in detail in Sections 2.4 and 2.5, respectively. The vertical component of the velocity (never computed later) can be determined by using the incompressibility of ice. Where there is no ice ($h = 0$), \mathbf{u}_{TOT} , \mathbf{u}_{SIA} , and \mathbf{u}_{SSA} are arbitrarily set to zero.

2.3. Mass conservation

The mass conservation principle in a non-empty vertical column of ice can be written as [21,31]

$$\frac{\partial h}{\partial t} + \nabla \cdot \mathbf{q}_{TOT} = a, \quad (3)$$

where $a = a(\mathbf{x})$ is the yearly-averaged positive or negative external ice mass balance due to melting and solid precipitation, and

$$\mathbf{q}_{TOT} := \int_l^s \mathbf{u}_{TOT}(z) dz = \int_l^s \mathbf{u}_{SIA}(z) dz + h \mathbf{u}_{SSA} =: \mathbf{q}_{SIA} + \mathbf{q}_{SSA} \quad (4)$$

defines the total horizontal ice flux that can be split into \mathbf{q}_{SIA} and \mathbf{q}_{SSA} which derive from \mathbf{u}_{SIA} and \mathbf{u}_{SSA} , respectively. Eq. (3) says that the variation of ice thickness plus the divergence of the ice flux equals the external ice mass balance.

Note that $h \geq 0$ on Ω and Eq. (3) acts only over $\Omega_+ := \{\mathbf{x} \in \Omega, h(\mathbf{x}) > 0\}$. In contrast, two case might occur where there is no ice (on $\Omega \setminus \Omega_+$): (i) a is negative and h remains to zero, (ii) a is positive and h increases with respect to a , the two being summarized by the following relation:

$$\frac{\partial h}{\partial t} = \max(a, 0) \quad \text{on } \Omega \setminus \Omega_+. \quad (5)$$

Note that $\mathbf{q}_{SIA} = \mathbf{q}_{SSA} = \mathbf{0}$ on $\Omega \setminus \Omega_+$.

2.4. Shallow Ice Approximation (SIA)

The isothermal SIA model describes the velocity profile \mathbf{u}_{SIA} as a function of the ice thickness h , the vertical component z , the surface elevation s and its gradient ∇s [21,31]:

$$\mathbf{u}_{SIA}(\mathbf{x}, z, t) = -(2A/p)(\rho g)^{p-1} [h^p - (s - z)^p] |\nabla s|^{p-2} \nabla s, \quad (6)$$

where $A > 0$ is the ice softness, p is a constant exponent linked to Glen's exponent \bar{n} by the relation $p = \bar{n} + 1$ and $|\cdot|$ denotes the Euclidean norm. The most realistic value for \bar{n} is found empirically close to 3 [31], consequently we assume $p > 2$. Using (4) and (6), the contribution of the SIA component to the horizontal ice flux is

$$\mathbf{q}_{SIA} = \int_l^s \mathbf{u}_{SIA}(z) dz = -\Gamma h^{p+1} |\nabla s|^{p-2} \nabla s, \quad (7)$$

where $\Gamma = 2A(\rho g)^{p-1}/(p+1) > 0$.

Eqs. (3) and (4) yield a single partial differential equation for the surface elevation h on Ω_+

$$\frac{\partial h}{\partial t} + \nabla \cdot \mathbf{q}_{SIA} + \nabla \cdot (h \mathbf{u}_{SSA}) = a. \quad (8)$$

On $\partial\Omega_+$, we might have $h(\mathbf{x}) > 0$ if there is an ice cliff (in Ω) or if there is an ice divide (at $\partial\Omega$). In both cases, we impose that the surface slope vanishes, i.e.

$$\nabla s \cdot \mathbf{n} = 0, \quad \text{on } \partial\Omega \cap \partial\Omega_+, \quad (9)$$

such that, from (7), we have a zero-SIA-flux at the boundary of the ice domain:

$$\mathbf{q}_{SIA} \cdot \mathbf{n} = 0, \quad \text{on } \partial\Omega_+. \quad (10)$$

Let $\varphi \geq 0$ be a test function, and apply Gauss theorem:

$$\int_{\Omega_+} \nabla \cdot \mathbf{q}_{SIA}(\varphi - h) dV = - \int_{\Omega_+} \mathbf{q}_{SIA} \cdot \nabla(\varphi - h) dV + \int_{\partial\Omega_+} (\varphi - h) \mathbf{q}_{SIA} \cdot \mathbf{n} dS.$$

The last boundary term vanishes because of (10). It follows from (8):

$$\int_{\Omega_+} \frac{\partial h}{\partial t}(\varphi - h) dV - \int_{\Omega_+} \mathbf{q}_{SIA} \cdot \nabla(\varphi - h) dV + \int_{\Omega_+} \nabla \cdot (h \mathbf{u}_{SSA})(\varphi - h) dV = \int_{\Omega_+} a(\varphi - h) dV. \quad (11)$$

Following [25], we want to rewrite our problem as an obstacle problem on the entire domain Ω which incorporates the free-boundary constraint through the condition $h \geq 0$. On $\Omega \setminus \Omega_+$, (5) implies (since $\varphi \geq h = 0$)

$$\int_{\Omega \setminus \Omega_+} \frac{\partial h}{\partial t} (\varphi - h) dV \geq \int_{\Omega \setminus \Omega_+} a(\varphi - h) dV. \quad (12)$$

Summing (11) and (12), we obtain the following variational inequality [25]:

$$\begin{aligned} \int_{\Omega} \frac{\partial h}{\partial t} (\varphi - h) dV + \Gamma \int_{\Omega} h^{p+1} |\nabla h + \nabla l|^{p-2} (\nabla h + \nabla l) \cdot \nabla (\varphi - h) dV \\ + \int_{\Omega} \nabla \cdot (h \mathbf{u}_{SSA}) (\varphi - h) dV \geq \int_{\Omega} a(\varphi - h) dV. \end{aligned} \quad (13)$$

Advantageously, the formulation (13) does not involve the unknown boundary of the ice domain $\{\mathbf{x} \in \Omega; h(\mathbf{x}) > 0\}$.

2.5. Shallow Shelf Approximation (SSA)

In the isothermal SSA model, the driving basal stress is partly balanced by the longitudinal stress (dominant at floating parts) and by the local stress at the base (dominant at grounding parts). More precisely, $\mathbf{u}_{SSA} = \mathbf{u}(\mathbf{x}, t)$ is determined by [36]

$$-A^{1-q} \nabla \cdot (h |D(\mathbf{u})|_*^{q-2} [D(\mathbf{u}) + \text{tr}(D(\mathbf{u}))I]) + C |\mathbf{u}|^{m-1} \mathbf{u} \times \mathbf{1}_{G(h)} = -\rho g h \nabla s, \quad \text{if } |\mathbf{u}| > 0, \quad (14)$$

$$\mathbf{u} = \mathbf{0}, \quad \text{else}, \quad (15)$$

where $q = p/(p-1) \in (1, 2)$ is the conjugate exponent to p , $\mathbf{1}_{G(h)}$ is a bi-valued function equal to one in the grounded part

$$G(h) := \{\mathbf{x} \in \Omega, b(\mathbf{x}) + (\rho/\rho_w)h(\mathbf{x}, \cdot) > 0, h(\mathbf{x}, \cdot) > 0\}, \quad (16)$$

and to zero outside $G(h)$, $D(\mathbf{u}) := \frac{1}{2}(\nabla \mathbf{u} + \nabla \mathbf{u}^T)$ denotes the strain rate of \mathbf{u} , tr is the trace operator, I the identity second order tensor and $|\cdot|_*$ denotes the norm $|X|_* := \sqrt{(X, X)_*}$ associated with the scalar product defined by

$$(X, Y)_* := \frac{1}{2}(\text{tr}(XY) + \text{tr}(X)\text{tr}(Y)).$$

Here, $m \geq 0$ is a given parameter and $C = C(\mathbf{x}) > 0$ is a prescribed bed yield stress. The term $\mathbf{1}_{G(h)}$ in Eq. (14) vanishes outside $G(h)$ since no basal shear stress occurs under the ice shelf. Heuristically, the first term in (14) represents the longitudinal stresses, the second term represents the friction on the bedrock and the right-hand-side represents the gravitational driving force. The case $m = 0$ corresponds to the “plastic” Coulomb-type law in [38]. Note that if $A = 0$, $m > 0$, and without shelf, Eq. (14) can be rewritten as $\mathbf{u} = -\frac{1}{C}(\rho g h |\nabla s|)^{1/m}$ corresponding to Weertman’s local sliding law [21]. Conditions on the boundary of the domain of ice $\partial\Omega_+$ change if there is still ice, if this ice is floating, grounded above or below sea level [36,43]. However, such boundary conditions can be written in a unified way:

$$A^{1-q} h |D(\mathbf{u})|_*^{q-2} [D(\mathbf{u}) + \text{tr}(D(\mathbf{u}))I] \cdot \mathbf{n} = \underbrace{\frac{1}{2} \rho g \left(h^2 - \frac{\rho_w}{\rho} [\min\{l, 0\}]^2 \right)}_{:= \mathbf{F}(h)} \mathbf{n}, \quad (17)$$

where l is defined by (1). Three cases might occur on the boundary $\partial\Omega_+$ in Eq. (17):

- (i) Ice is grounded above sea level, then $\mathbf{F}(h) = \frac{1}{2} \rho g h^2 \mathbf{n}$.
- (ii) Ice is grounded below sea level, then $\mathbf{F}(h) = \frac{1}{2} \rho g (h^2 - \frac{\rho_w}{\rho} b^2) \mathbf{n}$.
- (iii) Ice is floating, then $\mathbf{F}(h) = \frac{1}{2} \rho g h^2 (1 - \frac{\rho}{\rho_w}) \mathbf{n}$.

Clearly, if there is no ice ($h = 0$), then $\mathbf{F}(h) = \mathbf{0}$. The case (i) almost never appears in reality, since vertical ice cliffs are most of the time induced by the presence of water and calving processes. In the other cases, condition (17) says that the outward pressure of ice is partially balanced by the hydrostatic sea water pressure [36].

Multiplying (14) by $\mathbf{v} - \mathbf{u}$ where \mathbf{v} is a test function, integrating over Ω_+ , using Gauss theorem, the boundary condition (17), the equality $[D(\mathbf{u}) + \text{tr}(D(\mathbf{u}))I] \cdot \nabla(\mathbf{v} - \mathbf{u}) = (D(\mathbf{u}), D(\mathbf{v} - \mathbf{u}))_*$ and the convexity of function $s \rightarrow |s|^{m+1}$, lead to the variational inequality [36]

$$\begin{aligned}
& A^{1-q} \int_{\Omega} h |D(\mathbf{u})|_*^{q-2} (D(\mathbf{u}), D(\mathbf{v} - \mathbf{u}))_* dV + \frac{1}{m+1} \int_{G(h)} C(|\mathbf{v}|^{m+1} - |\mathbf{u}|^{m+1}) dV \\
& + \rho g \int_{\Omega} h \nabla s \cdot (\mathbf{v} - \mathbf{u}) dV - \int_{\partial\Omega_+} \mathbf{F}(h) \cdot (\mathbf{v} - \mathbf{u}) dS \geq 0.
\end{aligned} \tag{18}$$

In the variational inequality (18), the three first integrals can be indifferently written on Ω or Ω_+ since $h = 0$ on $\Omega \setminus \Omega_+$. In contrast, one needs to identify the boundary $\partial\Omega_+$ to compute the last term, which corresponds to an interior ice cliff. Note that, the inequality (18) can be actually rewritten as a variational equality [38] when $m > 0$.

2.6. Whole problem

For a given initial condition $h(\cdot, 0) = h_0(\cdot)$, our goal is to find $h(\cdot, t)$ and $\mathbf{u}(\cdot, t)$ that solve the system of Eqs. (13), (18) for $t \in [0, T]$. The next section is dedicated to the approximation of solutions for this system.

In what follows, we refer to “SSA + SIA” the entire model presented here and to “SSA” when taking $\mathbf{u}_{SIA} = \mathbf{0}$ instead of (6).

3. Approximations

3.1. Time approximation

Let $N > 0$ be given, and $[t_0, \dots, t_{N+1}]$ be a time discretization of $[0, T]$ with time steps $\tau_n = t_{n+1} - t_n$, $n = 0, 1, \dots, N$. Let us denote by $h_n, l_n, s_n, \mathbf{u}_n$ some time approximations of $h(t_n), l(t_n), s(t_n)$ and $\mathbf{u}(t_n)$ for all $n = 0, 1, \dots, N + 1$.

First we note that the variational inequality (18) for the SSA part can be rewritten as a minimization problem [36] (step I below). The variational inequality (13) for the SIA part is derived from a nonlinear diffusion–advection equation (8) that is expected to be advection-dominated on the floating part and diffusion-dominated on the grounded part. Operator splitting techniques [14, Ch. 2] for solving (13) are used to decouple the advection operator from the diffusion operator. A first order operator splitting corresponds to solving the equation, first without diffusion with appropriate initial conditions and second without the advection term and source terms. Using this operator splitting for a semi-implicit discretization of (13) leads to a transport problem (step II below) and a variational inequality that can also be written as a minimization problem [25] (step III below). Finally, assuming h_n known for some n , the three steps below describe how to compute h_{n+1} .

Step I: Find \mathbf{u}_n that minimizes

$$\mathcal{J}_{SSA}(\mathbf{v}) := \frac{2A^{1-q}}{q} \int_{\Omega} h_n |D(\mathbf{v})|_*^q dV + \frac{1}{m+1} \int_{G(h_n)} C|\mathbf{v}|^{m+1} dV + \rho g \int_{\Omega} h_n \nabla s_n \cdot \mathbf{v} dV - \int_{\partial\Omega_+^n} \mathbf{F}(h_n) \cdot \mathbf{v} dS, \tag{19}$$

where $s_n = l_n + h_n$, l_n is computed from (1) with h_n and $\Omega_+^n = \{\mathbf{x} \in \Omega, h_n(\mathbf{x}) > 0\}$.

Step II: Find $h_{n+\frac{1}{2}}$, the solution at time t_{n+1} of the advection problem

$$\begin{cases} \frac{\partial h}{\partial t} + \nabla \cdot (h \mathbf{u}_n) = 0, & \text{on } (t_n, t_{n+1}), \\ h(t_n) = h_n. \end{cases} \tag{20}$$

Step III: Find $h_{n+1} \geq 0$ that minimizes over all $\varphi \geq 0$

$$\mathcal{J}_{SIA}(\varphi) := \frac{1}{2\tau_n} \int_{\Omega} \varphi^2 dV + \frac{\Gamma}{p} \int_{\Omega} (h_{n+\frac{1}{2}})^{p+1} |\nabla \varphi + \nabla l_{n+\frac{1}{2}}|^p dV - \int_{\Omega} \left(\frac{h_{n+\frac{1}{2}}}{\tau_n} + a \right) \varphi dV, \tag{21}$$

where $l_{n+\frac{1}{2}}$ is computed from (1).

If one does not need to account for the SIA velocity in our model (“SSA” model, i.e. $\mathbf{u}_{SIA} = \mathbf{0}$), step III is simply replaced by

$$h_{n+1} = \max(h_{n+\frac{1}{2}} + a\tau_n, 0).$$

One can show that the functional \mathcal{J}_{SSA} is convex, strongly continuous in $W^{1,q}(\Omega)$ and therefore lower semicontinuous [36,38]. Using the second Korn inequality [36], one can prove the coerciveness of \mathcal{J}_{SSA} , and then the existence of a minimizer if h_n is uniformly lower bounded by a positive constant and $m > 0$ [36,38]. In addition, this minimizer is unique if $G(h_n)$ has a positive measure. The case $m = 0$, namely Coulomb friction or “plastic till”, requires further hypothesis [38]. In the same way, one can show that \mathcal{J}_{SIA} is strictly convex, coercive, strongly continuous in $\{v \in W^{1,p}(\Omega), v \geq 0\}$ and then lower semicontinuous [25] if $h_{n+\frac{1}{2}}$ is uniformly lower bounded. However, since h_n and $h_{n+\frac{1}{2}}$ can be equal to zero, the two minimization problems are not guaranteed to be well-posed.

3.2. Space approximation

The minimization problems of steps I and III both derive from a nonlinear p -Laplace problem, however, with $q < 2$ in step I and $p > 2$ in step III. Finite element approximations of p -Laplace problems were proposed and analyzed in [3]. More specifically, the obstacle problem resulting from the mass conservation and the SIA in a steady state shape (similar to the one of step III) was treated in [25]. Likewise, the problem of step I was analyzed in [38]. Multigrid algorithms for the p -Laplace problem have been proposed and analyzed in [4,23]. There are two basic approaches to implement multigrid methods for convex nonlinear minimization problems [28]. The first approach consists of linearizing the problem and using a multigrid solver for the remaining linear problems. This strategy was adopted in [23], where multigrid was used to solve the linearized subproblems in a damped Newton-like descent method. The second approach applies the multigrid methodology directly in the original nonlinear equation with a nonlinear smoother. As an example, the full approximation scheme with a Polak–Ribiere conjugate gradient method as smoother was applied in [4]. An obstacle constraint induces an additional nonsmooth nonlinearity that cannot be directly tackled by a Newton-type method that requires smoothness. To account for nonsmooth nonlinearities, we need to use some additional methods such as primal–dual active set or truncated monotone multigrid [17,27]. In Section 3.2.1, we adopt a closely related approach, more precisely, the Truncated Nonsmooth Newton MultiGrid (TNNMG) method [16–18].

A number of schemes exist to solve the transport problem (20) (step II) including finite differences [7,43], finite elements [11] or finite volumes [12]. We opt for the latter and discuss the details in Section 3.2.2.

Assume \mathcal{T}_h to be a mesh of $\Omega \subset \mathbb{R}^{d-1}$, that is made of segments when $d = 2$ and of triangles when $d = 3$. The mesh \mathcal{T}_h is parametrized by h , the size of its highest diameter element, and satisfies three fundamental assumptions. First, we assume that \mathcal{T}_h is *regular* in the sense that it consists of a finite number of non-degenerate simplices. Second, we assume the mesh to be *conforming* [13], i.e. the intersection of any pair of element boundaries is either empty or a common vertex or edge of the two elements. Third, we suppose \mathcal{T}_h to be *hierarchical* (or *multilevel*), i.e. \mathcal{T}_h results from several levels of local or global refinement applied to an initial coarse mesh of Ω . Such hierarchy is necessary to apply the geometric multigrid method in Section 3.2.1. Since we implement an adaptive mesh refinement procedure in Section 3.2.3, the mesh \mathcal{T}_h changes with the time step n , i.e. $\mathcal{T}_h = \mathcal{T}_{h,n}$. For simplicity, we omit the dependence on n until Section 3.2.3.

We now introduce some notations related to \mathcal{T}_h that will be used in Sections 3.2.1 and 3.2.2. The mesh \mathcal{T}_h contains I nodes $\{\mathbf{p}_i\}_{i=1,\dots,I} \subset \mathbb{R}^{d-1}$ and L elements $\{e_l\}_{l=1,\dots,L}$. We will later consider the finite element space \mathcal{V}_h spanned by the continuous, linear on each element of \mathcal{T}_h functions λ_i , defined by $\lambda_i(\mathbf{p}_j)$ equals one if $i = j$ and zero else. We call $h_{h,n}$, $l_{h,n}$, $s_{h,n} \in \mathcal{V}_h$ and $\mathbf{u}_{h,n} \in \mathcal{V}_h^{d-1}$ some approximations in space of h_n , l_n , s_n and \mathbf{u}_n . The approximation $h_{h,n}$ can be identified with the set of nodal values $\{H_i, i = 1, \dots, I\}$ for the finite element space \mathcal{V}_h since (dropping n) $h_h = \sum_{i=1,\dots,I} H_i \lambda_i$. The same identification holds for $l_{h,n}$, $s_{h,n}$ and $\mathbf{u}_{h,n}$.

3.2.1. Minimization problems (steps I and III)

The Ritz–Galerkin approximation of the first minimization problem (step I) in this finite element space $[\mathcal{V}_h]^{d-1}$ can be written directly in the following form:

$$\text{Find } \mathbf{U} = \{\mathbf{U}_i\}_{i=1,\dots,I} \in [\mathbb{R}^I]^{d-1} \quad \text{s.t.} \quad \mathcal{J}_{SSA}^h(\mathbf{U}) \leq \mathcal{J}_{SSA}^h(\mathbf{V}), \quad \forall \mathbf{V} \in [\mathbb{R}^I]^{d-1},$$

where

$$\mathcal{J}_{SSA}^h(\mathbf{V}) := \sum_{l=1}^L \alpha_l \left| \sum_{j \in e_l} \mathbf{V}_j D_{|e_l|}(\lambda_j) \right|_*^q + \sum_{i=1}^I \beta_i |\mathbf{V}_i|^{m+1} + \sum_{i=1}^I \mathbf{G}_i \cdot \mathbf{V}_i - \sum_{i=1}^I \mathbf{F}_i \cdot \mathbf{V}_i, \quad (22)$$

and

$$\begin{aligned} \alpha_l &:= \frac{2A^{1-q}}{q} \int_{e_l} h_{h,n} dV, & \beta_i &:= \frac{1}{m+1} \int_{G(h_n)} C \lambda_i dV, \\ \mathbf{G}_i &:= \rho g \int_{\Omega} h_{h,n} \nabla s_{h,n} \lambda_i dV, & \mathbf{F}_i &:= \int_{\partial \Omega_+^n} \mathbf{F}(h_{h,n}) \lambda_i dS. \end{aligned} \quad (23)$$

In the same way, the Ritz–Galerkin approximation of the second minimization problem (step III) in the same finite element space \mathcal{V}_h can be written as:

$$\text{Find } H = \{H_i\}_{i=1,\dots,I} \in \mathbb{R}^I \quad \text{s.t.} \quad \mathcal{J}_{SIA}^h(H) \leq \mathcal{J}_{SIA}^h(\Phi), \quad \forall \Phi \in \mathbb{R}^I,$$

where

$$\mathcal{J}_{SIA}^h(\Phi) = \sum_{i=1}^I \gamma_i \Phi_i^2 + \sum_{l=1}^L \mu_l \left| \sum_{j \in e_l} (\Phi_j + l_{n+\frac{1}{2},j}) \nabla_{|e_l|} \lambda_j \right|^p - \sum_{i=1}^I f_i \Phi_i + \sum_{i=1}^I \chi(\Phi_i), \quad (24)$$

and

$$\gamma_i := \frac{1}{2\tau_n} \int_{\Omega} \lambda_i dV, \quad \mu_i := \frac{\Gamma}{p} \int_{e_i} (h_{h,n+\frac{1}{2}})^{p+1} dV, \quad f_i := \int_{\Omega} \left(\frac{h_{h,n+\frac{1}{2}}}{\tau_n} + a \right) \lambda_i dV, \quad (25)$$

where χ is the function defined by $\chi(a) = \begin{cases} 0, & \text{if } a \geq 0, \\ +\infty, & \text{else.} \end{cases}$

Since $h_{h,n+\frac{1}{2}}$ and $s_{h,n+\frac{1}{2}}$ are linear on each element, the integrals α_i , \mathbf{G}_i , \mathbf{F}_i , γ_i and f_i in (23) and (25) can be computed exactly by using numerical quadratures with a sufficiently large order. This is also true for β_i if C is constant and for μ_i if p (or \bar{n}) is an integer. However, in practice, we use some approximations such that $\mathcal{J}_{SSA} \neq \mathcal{J}_{SSA}^h$ and $\mathcal{J}_{SIA} \neq \mathcal{J}_{SIA}^h$.

Eventually, the Ritz–Galerkin approximation of the two minimization problems (steps I and III) in the standard continuous linear finite element space can be written in a unified form:

$$\text{Find } U \in \mathbb{R}^J \text{ s.t. } \mathcal{J}(U) \leq \mathcal{J}(V), \quad \forall V \in \mathbb{R}^J, \quad (26)$$

where $J \in \mathbb{N}$, $\mathcal{J}: \mathbb{R}^J \rightarrow \mathbb{R} \cup \{+\infty\}$ is strictly convex, coercive, lower semicontinuous, but not necessary smooth. Indeed, the case $m=0$ in (22) or the function χ in (24) (generated by the obstacle) are two nonsmooth terms in \mathcal{J}_{SSA}^h and \mathcal{J}_{SIA}^h , respectively. Also, \mathcal{J}_{SSA}^h and \mathcal{J}_{SIA}^h are coercive in the finite dimensional space since all norms are equivalent.

Following the techniques that have been developed in [16–18] for linear and nonlinear problems with obstacle, we now describe the TNNMG method for minimization problems of type (26). The key assumption of the TNNMG method, as presented here, is that the nonsmooth part of the energy functional \mathcal{J} is separable, i.e. it decomposes with respect to the one-dimensional Euclidean directions. The latter is true for \mathcal{J}_{SIA}^h and, if $d=2$, also for \mathcal{J}_{SSA}^h .

Define the nonlinear Gauß–Seidel smoother $\mathcal{F}: \mathbb{R}^J \rightarrow \mathbb{R}^J$ by

$$\mathcal{F}(U)_i = \arg \min_{\rho \in \mathbb{R}} \mathcal{J} \left(U + \sum_{j=1}^{i-1} \mathcal{F}(U)_j E_j + \rho E_i \right), \quad \forall i = 1, \dots, J, \quad (27)$$

where $\{E_i, i = 1, \dots, J\}$ denotes the canonical base of \mathbb{R}^J . One Gauß–Seidel iteration consists of minimizing successively \mathcal{J} in all coordinate directions. Here, the nonlinear scalar minimization problems (27) are solved inexactly by using a bisection method which does not require any smoothness on \mathcal{J} .

For $d=3$ the nonsmooth part in \mathcal{J}_{SSA}^h does only decouple into local two-dimensional problems because of the Euclidean norm $|\cdot|$ in (22). In this case the TNNMG method as introduced below will in general only converge if the Gauß–Seidel method is replaced by a block Gauß–Seidel method solving local two-dimensional problems. For simplicity we omit the details and restrict ourselves to $d=2$ if $m=0$ in the following.

The TNNMG method defines a sequence $\{U^v\}$ by

$$U^{v+\frac{1}{2}} = U^v + \mathcal{F}(U^v), \quad (28)$$

$$\mathcal{I}^v = \mathcal{I}(U^{v+\frac{1}{2}}), \quad (29)$$

$$V^{v+\frac{1}{2}} = -(\mathcal{J}''(U^{v+\frac{1}{2}})_{\mathcal{I}^v, \mathcal{I}^v})^\dagger \mathcal{J}'(U^{v+\frac{1}{2}})_{\mathcal{I}^v}, \quad (30)$$

$$V^{v+1} = \mathcal{P}_{\text{Dom}(\mathcal{J}) - U^{v+\frac{1}{2}}} (V^{v+\frac{1}{2}}), \quad (31)$$

$$U^{v+1} = U^{v+\frac{1}{2}} + \rho^v V^{v+1}, \quad (32)$$

where

$$\rho^v = \arg \min_{\rho \in [0, \infty)} \mathcal{J}(U^{v+\frac{1}{2}} + \rho V^{v+1}), \quad (33)$$

$$\mathcal{I}(V) = \{i: \text{the subdifferential } \partial \mathcal{J}(V_i) \text{ is single-valued}\}, \quad (34)$$

and where $N_{\mathcal{I}}$ and $M_{\mathcal{I}, \mathcal{I}}$ are the vectors and matrices truncated to the set of indices \mathcal{I} for any vector N and any matrix M , i.e. the elements of the i -th line (and i -th column of the matrix) that are not in \mathcal{I} are set to zero. Here, $\mathcal{P}_{\text{Dom}(\mathcal{J}) - U}$ denotes the projection on the convex set $\text{Dom}(\mathcal{J}) - U = \{V: \mathcal{J}(U + V) < +\infty\}$.

Step (28) consists of one smoother iteration that successively minimizes the energy functional in the scalar coordinate directions. Then the inactive set \mathcal{I}^v is selected (29), such that \mathcal{J} is (locally) smooth on the subspace

$$\mathbb{R}_{\mathcal{I}^v}^J := \{V \in \mathbb{R}^J, V_i = 0 \text{ if } i \notin \mathcal{I}^v\} \quad (35)$$

spanned by the inactive components. The $(\cdot)^\dagger$ in step (30) denotes the Moore–Penrose pseudoinverse [40] which is effectively the inverse on the subspace $\mathbb{R}_{\mathcal{I}^v}^J$, such that (30) is a Newton correction on this subspace. Note that, due to the selection of \mathcal{I}^v , all necessary derivatives of \mathcal{J} exist on this subspace. Since the application $U^{v+\frac{1}{2}} + V^{v+\frac{1}{2}}$ of the Newton

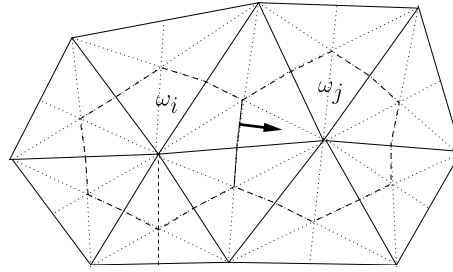


Fig. 2. Illustration of vertex-centred finite volumes when $d = 3$. A few elements of the mesh \mathcal{T}_h are represented with continuous bold lines, the medians of all triangles are drawn with dotted lines and two finite volumes ω_i and ω_j are represented with dashed lines.

correction might lead outside the convex set $\text{Dom}(\mathcal{J})$, the projection step (31) is advocated to constrain the new iterate to remain in $\text{Dom}(\mathcal{J})$. Since the projected correction does not necessarily decrease the energy, a damping parameter in step (32) ensures the monotonicity of the scheme and the global convergence of the method [17]. It remains to describe how to invert $\mathcal{J}''(U^{v+\frac{1}{2}})_{\mathcal{T}^v, \mathcal{T}^v}$ in step (30). Multigrid methods are known to be one of the fastest approaches to solve linear systems resulting from discretized partial differential equations [22,44]. A remarkable feature of multigrid methods are mesh-independent convergence rates. Since the matrix $\mathcal{J}''(U^{v+\frac{1}{2}})_{\mathcal{T}^v, \mathcal{T}^v}$ is symmetric and positive definite on the subspace $\mathbb{R}_{\mathcal{T}^v}^I$, we can apply a linear geometric multigrid method for the inversion of $\mathcal{J}''(U^{v+\frac{1}{2}})_{\mathcal{T}^v, \mathcal{T}^v}$ in the correction step (30).

The hierarchical (or multilevel) aspect of the mesh \mathcal{T}_h is crucial for the application of a geometric multigrid method. Indeed, such method relies on sequentially nested grids and the application of simple relaxation methods at all levels of the grid hierarchy. While a smoother on a fine grid is efficient to reduce the high frequencies of the error, the low frequencies are more efficiently damped on coarser grids [44]. The multigrid method consists of the application of a smoother on all finite element spaces induced by the grids of the hierarchy in order to damp all frequencies of the error. As a special feature the matrix $\mathcal{J}''(U^{v+\frac{1}{2}})_{\mathcal{T}^v, \mathcal{T}^v}$ is in general only positive semi-definite on the whole space \mathbb{R}^I . The fact that the matrix is not invertible in general does not pose a problem since a standard linear multigrid method will automatically act on the space $\mathbb{R}_{\mathcal{T}^v}^I$ and implicitly use subspaces of $\mathbb{R}_{\mathcal{T}^v}^I$ for the coarse grid corrections [16].

We opt for a V-cycle type multigrid solver combined with a linear Gauß–Seidel smoother with 3 pre- and post-smoothing steps [22]. Since there is no need to solve the system (30) to a certain accuracy, applying one single multigrid iteration is enough to reach global convergence. The implementation is based on the code *DUNE* (<http://www.dune-project.org/dune.html>) and the modules *Dune-Solvers* and *Dune-Tnmng* [18].

The convergence of the TNNMG method for strongly convex energy functionals was proven in [16] for the Gauß–Seidel smoother defined by (27) and a variant with inexact solution of the scalar subproblems in (27). A generalization of the proof for strictly convex functionals is given in [20]. The convergence result remains true when replacing the nonlinear Gauß–Seidel smoother by the simpler Jacobi smoother, however, a damping must be advocated in step (28) to insure the global convergence.

Some numerical results to test the performance of the TNNMG method are given in Section 4.4.

3.2.2. Transport problem (step II)

In this section, we briefly describe how to solve (20) using a finite volume method [30]. The exact mass conservation is an attractive feature of this method. Since h_n takes nodal values, we opt for vertex-centered finite volumes. In one space dimension ($d = 2$), the finite volume at a given node is simply delimited by the midpoints of neighboring cells. In two space dimensions ($d = 3$), finite volumes are built by following the medians of all triangles, see Fig. 2. As an alternative, one could follow a strategy using Voronoi cell structures like in [12].

If we call ω_i the finite volume that is centred at node i , the value of h_n on ω_i used for the transport scheme is identified to its nodal value $h_n(\mathbf{p}_i)$ defined in Section 3.2. With this identification, h_n does not need to be interpolated. We opt for a full upwind evaluation of the fluxes and an explicit Euler scheme in time. When $d = 2$, this scheme is strictly equivalent to the classical explicit upwind finite difference scheme, like the one used in [43]. For stability reason, this scheme cannot be performed with too large time step τ_n . The time step is then computed adaptively such that the CFL condition is fulfilled.

3.2.3. Fixed and adaptive grid strategies

Ice sheets exhibit strong variations of velocities between slow grounded parts and fast floating parts, i.e. in the neighborhood of the Grounding Line (GL). Therefore, using a fixed mesh, it might be very expensive to capture such sharp changes in the dynamical regime of ice [34] with a reasonable accuracy. Thus an adaptive mesh refinement procedure is implemented to obtain a high accuracy close to the GL while keeping the computational effort moderate. The finite element and finite volume techniques detailed in Sections 3.2.1 and 3.2.2 are combined with a heuristic local mesh refinement procedure based on the distance to the GL function. The presented adaptive scheme builds up a new mesh \mathcal{T}_h of Ω at each time step n before starting step I, i.e. $\mathcal{T}_h = \mathcal{T}_{h,n}$.

To apply the techniques detailed in Sections 3.2.1 and 3.2.2, such meshes must be regular, conforming, and hierarchic. By hierarchic, we mean that $\mathcal{T}_{h,n}$ is derived from a sequence of meshes $\{\mathcal{T}_j\}_{j=0,\dots,\bar{j}}$ such that the finite element spaces $\mathcal{S}_j = \text{span}\langle \lambda_i^j, i \in \mathcal{T}_j \rangle$ of continuous piecewise linear functions are hierarchically embedded, i.e.

$$\mathcal{S}_0 \subset \dots \subset \mathcal{S}_{\bar{j}}. \quad (36)$$

Here, $j \in \{0, \dots, \bar{j}\}$ denotes the level of \mathcal{T}_j or \mathcal{S}_j , where \bar{j} is the highest level and $\mathcal{T}_{\bar{j}} = \mathcal{T}_{h,n}$. Moreover, we construct this sequence of meshes $\{\mathcal{T}_j\}_{j=0,\dots,\bar{j}}$ such that they have a common trunk (independent of n):

$$\mathcal{T}_0, \dots, \mathcal{T}_{\bar{j}}, \quad (37)$$

and a specific branch (depending of n):

$$\mathcal{T}_{\bar{j}+1,n}, \dots, \mathcal{T}_{\bar{j},n}. \quad (38)$$

While the highest level $\mathcal{T}_{\bar{j}}$ of (37) must only capture the solution far from the GL, the highest level $\mathcal{T}_{\bar{j},n}$ in (38) must have a sufficiently small size to capture the expected sharp changes in the ice dynamics close to the GL. Later, the corresponding mesh sizes are denoted by h_{\max} and h_{\min} . In the two following paragraphs, we define how we construct the sequence of meshes (when $d=3$) in the common trunk (37) and of the specific branch (38), respectively.

The common trunk (37) is simply obtained from j successive uniform refinements of an initial mesh \mathcal{T}_0 . If Ω is polyhedral \mathcal{T}_0 can be a triangulation of Ω . The sequence $\{\mathcal{T}_j\}_{j=1,\dots,\bar{j}}$ is obtained by uniformly refinement, i.e., by splitting each triangle into four triangles, leading to a natural embedding (36) of the associated finite element spaces. However, if Ω is more general (for instance like the disk in Section 4.4), each \mathcal{T}_j is only a triangulation of a polyhedral approximation Ω_j of Ω . The latter is obtained by moving new vertices introduced on $\partial\Omega_{j-1}$ to $\partial\Omega$ during the construction of \mathcal{T}_j . While the finite element spaces associated to the \mathcal{T}_j do in general not satisfy (36), such nested sequence (36) can be easily be constructed via the isomorphism that identifies corresponding unmoved and moved vertices.

To build the adaptive meshes (38) at each time step n , we combine a heuristic marking strategy with classical red–green refinement starting from $\mathcal{T}_{\bar{j}}$ (and not from the last mesh $\mathcal{T}_{h,n-1}$). First we define the band

$$R_n = \{\mathbf{x}; \text{dist}(\mathbf{x}, GL_n) < L_f\}, \quad (39)$$

of width $L_f > 0$ around the GL at time t_n defined by

$$GL_n := \{\mathbf{x} \in \Omega, b(\mathbf{x}) + (\rho/\rho_w)h_n(\mathbf{x}, \cdot) = 0, h_n(\mathbf{x}, \cdot) > 0\}. \quad (40)$$

Then, we refine all triangles of the mesh whose the center of gravity is in R_n following the “red rule”, i.e. we split each triangle into four smaller children obtained by adding a new node at the center of all edges of the triangle.

Due to hanging nodes, the resulting mesh is non-conformal. As a remedy, we re-refine with the same “red rule” all the triangles containing more than one hanging node until this kind of triangle has totally vanished. Finally, we “close” all the triangles containing a single hanging node by applying the so-called “green rule”, i.e. the hanging node is connected to the opposed vertex. As a result, we obtain the mesh $\mathcal{T}_{\bar{j}+1,n}$. Unfortunately, applying the green refinement procedure deteriorates the regularity of the mesh because of the angle bisection. To prevent against degenerate triangles, we simply remove all closures (i.e. all triangles resulting from green refinement) before we re-refine at the next level such that green refinement is never applied more than once on the same triangle. The following levels $\{\mathcal{T}_{j,n}\}_{j=\bar{j}+2,\dots,\bar{j}}$ are built by continuing this procedure.

By construction, the refinement procedure guarantees the conformity and the regularity of all the mesh $\mathcal{T}_{j,n}$. Moreover, a hierarchy arises from the sequence $\{\mathcal{T}_{j,n}\}_{j=0,\dots,\bar{j}}$, which is essential to implement the geometrical multigrid method since it relies on a sequence of nested finite element of type (36). For $j = 0, \dots, \bar{j}$, refining uniformly gives rise to a natural sequence of nested finite element spaces (36). However, when applying local refinements, the resulting finite element spaces are in general no longer nested because of green refined elements. For this reason, we consider the meshes

$$\bar{\mathcal{T}}_j = \left\{ \tau \in \bigcup_{0 \leq k \leq j} : \begin{array}{l} \tau \text{ results from } j \text{ red refinements or} \\ \tau \text{ results from } k \leq j \text{ refinements and was never refined} \end{array} \right\}$$

in place of \mathcal{T}_j such that the spanned meshes are nested.

In addition to modify the mesh \mathcal{T}_h , the quantity h_{n-1} needs to migrate from the mesh $\mathcal{T}_{h,n-1}$ to the new one $\mathcal{T}_{h,n}$. This is done by computing the linear interpolation of h_{n-1} at the nodes in $\mathcal{T}_{h,n}$. In regions where the mesh was coarsened compared to $\mathcal{T}_{h,n-1}$, the function h_{n-1} can in general not be represented exactly on $\mathcal{T}_{h,n}$, resulting in quadrature errors in the integrals in (23) and (25). The latter can be avoided if both meshes, $\mathcal{T}_{h,n-1}$ and $\mathcal{T}_{h,n}$, are contained in a single, finer mesh hierarchy which will however introduce hanging nodes [19].

In Section 4, we refer to Fixed Grid (FG) strategy when using the uniform mesh directly without adaptation ($\bar{j} = \bar{j}$ or $h = h_{\min} = h_{\max}$) and to Adaptive Grid (AG) strategy when using the locally refined mesh ($\bar{j} < \bar{j}$ or $h_{\min} < h_{\max}$).

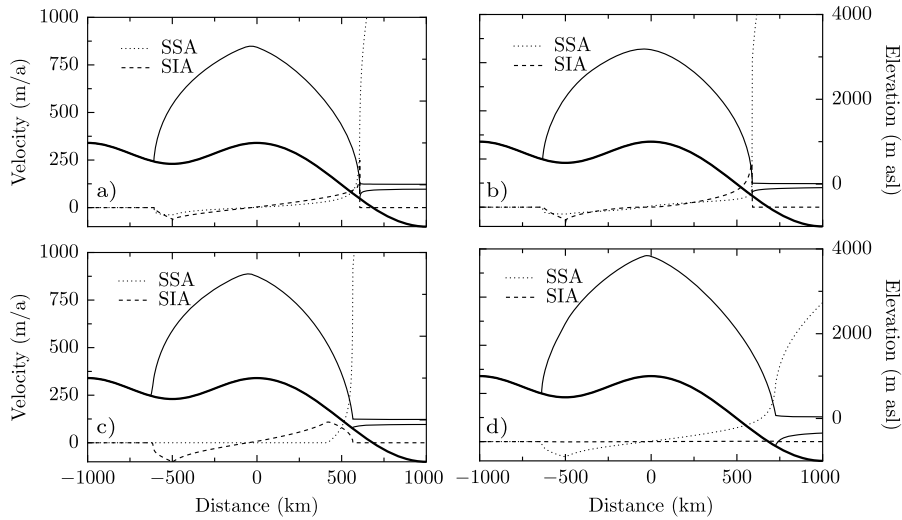


Fig. 3. Steady state shapes, SIA and SSA components of the velocity for the various parameterizations of experiments (a), (b), (c) and (d), see Table 1.

Table 1

Parameters for experiments (a), (b), (c), and (d). The units of C and A are $\text{Pa m}^{-m} \text{s}^m$ and $\text{Pa}^{-3} \text{s}^{-1}$, respectively.

	Experiment			
	(a)	(b)	(c)	(d)
m	$1/3$	1	0	$1/3$
C	7.624×10^6	7.208×10^{10}	1.0×10^5	7.624×10^6
A	4.6416×10^{-24}	4.6416×10^{-24}	4.6416×10^{-24}	4.6416×10^{-26}

4. Results

In this section, we perform several simulations of idealized two- and three-dimensional ice sheets. First, a two-dimensional ice sheet with an attached shelf part is simulated until reaching a steady state shape. We analyze the behavior of the SIA and SSA velocities and of the Grounding Line (GL) according to sliding and ice softness parameters. Second, we follow the test problems proposed in the Marine Ice Sheet Model Intercomparison Project (MISMIP) 2D [34] and we validate our results against an analytic solution. Then, we show some results related to the three-dimensional version of MISMIP, called MISMIP 3D [33]. Eventually, we perform some stationary computations of the SSA equation (15) to evaluate the performance of the TNNMG method. In the paper, the following physical parameters are used: $\rho = 900 \text{ kg m}^{-3}$, $\rho_w = 1000 \text{ kg m}^{-3}$, $\bar{n} = 3$ (or $p = 4$), and $g = 9.81 \text{ m s}^{-2}$.

4.1. Influence of sliding and ice softness parameters

Let us consider the one-dimensional domain $\Omega = [-1000, 1000] \text{ km}$ with the analytic curved bedrock as depicted in Fig. 3. We assume a bi-valued constant-in-time mass balance defined by $a(x) = -1 \text{ m y}^{-1}$ if $x < -500 \text{ km}$ and $a = 0.3 \text{ m y}^{-1}$ elsewhere. On the left-hand side of the domain Ω , the ablation area allows a free grounded margin to shape on the bedrock which is above sea level. On the right-hand side, the bedrock is below sea level and the mass balance is positive such that a shelf is generated up to the boundary of Ω . Four experiments are performed with the “SSA + SIA” model and different sets of parameters, see Table 1. As sliding law in Eq. (14), experiments (a) and (d) involve a power-type law, experiment (b) involves a linear-type law and experiment (c) involves a Coulomb-type law like in [36,38]. Experiment (d) corresponds to (a), however, with a much smaller parameter A (corresponding to a more viscous ice). For each experiment, we initialize the ice geometry by a ten-meter-thick layer of ice (grounded and floating) on Ω and run the model until reaching a steady state shape. For the discretization we adopt an FG strategy, i.e. the domain Ω is uniformly refined with a fine resolution: $h \sim 2 \text{ km}$, which corresponds to $j = \bar{j} = 10$ levels of refinements.

Ice sheets are considered to be steady when the normalized annual volume change is lower than 10^{-6} . Steady state shapes for experiments (a), (b), (c), and (d) were found after ~ 11 , ~ 18 , ~ 18 and ~ 20 millenniums, respectively. Fig. 3 displays the corresponding shapes with SIA and SSA velocity components. In contrast to the SSA velocities that were found by solving Eq. (18), the SIA velocity was obtained *a posteriori* from Eq. (6). Indeed, due to the inclusion of (6) in (3), there is no need to compute SIA velocities explicitly.

As expected, SSA velocities are dominant in the ice shelf. In contrast, SIA velocities play a significant role on the grounded part only when the gradient of the top surface elevation is sufficiently large and when A is not too small (Eq. (6)). Power

Table 2MISMIP 2D parameters. Unit for C is $\text{Pa m}^{-m} \text{ s}^m$.

Experiment	Bedrock			
	Sloppy-flat bed, Eq. (41)		Polynomial bed, Eq. (42)	
	(1a/2a)	(1b/2b)	(3a)	(3b)
m	1/3	1	1/3	1
C	7.624×10^6	7.208×10^{10}	7.624×10^6	7.208×10^{10}

or linear parameterizations of the sliding do not show major differences in ice velocities. However, the highest part of the steady ice sheet is smooth with the linear law while there is a visible jump in the derivatives with the power law corresponding to the well-known Raymond bump [35]. In contrast to power or linear laws, the Coulomb-type law displays SSA velocities only in the transition and floating areas. As expected, there is clear separation between zero SSA velocity and non-zero SSA velocity. Also, linear and power sliding laws induce steeper gradients of the top surface elevation at the Grounding Line (GL) position. In particular, this is visible at the GL, since both laws exhibit SIA velocities that tend to infinity (or, equivalently, the gradient of the top surface tends to infinity, see Eq. (6)). In contrast, the Coulomb sliding law exhibits regular SIA velocities. As expected, taking a smaller A reduces both SSA and SIA velocities such that the ice sheet gets thicker and the GL stabilizes further from the origin. This can also be observed when comparing the experiments (a) and (d) in Fig. 3. Simulating the effects of several values of A on the GL is the goal of the next section.

4.2. MISMIP 2D

The Marine Ice Sheet Model Intercomparison Project MISMIP (2D) consists of several simulation runs of a two-dimensional ice sheet and ice shelf that have been designed to allow a better comparison between marine ice sheet models [34]. In particular, the project aims to test the reversibility of the modeled Grounding Line (GL), i.e. its ability to recover its location after a perturbation in flow law parameters. This reversibility is physical on a downward-sloping bedrock. However, it is known that no GL can stabilize—and then be reversible—on upward-sloping bedrock [37]. Indeed, the ice discharge through the GL increases with the ice thickness [37]. As a consequence, any slight retreat of the GL on an upward-sloping bed would increase the ice thickness at the GL, increase the flux, and enhance the retreat. By such positive feedback effect, a marine ice sheet might retreat in an irreversible way if a depression occurs on the bedrock. Such phenomenon—called hysteresis—is also a part of the MISMIP experiments.

We consider the one-dimensional domain $\Omega = [0, 2000]$ km. There are four experiments in MISMIP that differ by the choice of the bedrock, parameters C and m and by a set of parameters A , see Table 2. We use the labels 1a/2a, 1b/2b, 3a, and 3b, as originally introduced in [34]. On the one hand, experiments 1a/2a and 1b/2b use a bedrock with a constant slope while experiments 3a and 3b use a polynomial bedrock. They are respectively defined by

$$b(x) = 720 - 778.5 (x/\bar{L}), \quad (41)$$

$$b(x) = 729 - 2184.8 (x/\bar{L})^2 + 1031.72 (x/\bar{L})^4 - 151.72 (x/\bar{L})^6, \quad (42)$$

where $\bar{L} = 750$ km. On the other hand, experiments 1a/2a and 3a use a power-type sliding parametrization while experiments 1b/2b and 3b use a linear-type sliding parametrization. The accumulation rate is taken as constant, $a = 0.3 \text{ m a}^{-1}$, for all experiments. Note that, symmetry is imposed at $x = 0$ km.

MISMIP experiments aim to model several steady state shapes that correspond to a given set of decreasing parameters $\{A_i, i = 1, \dots, J\}$ for the ice softness, see [34]. The following procedure is applied to each experiment:

- **Initialize** the geometry with a ten-meter-thick ice sheet and ice shelf.
- **For** $i = 1, 2, \dots, J - 1, J, J - 1, \dots, 2, 1$, run the model with A_i as ice softness parameter until reaching a steady shape.

First, we use a constant thin layer of ice as an initial geometry and run the model with the highest parameter A_1 until reaching a steady shape. Then, A_i is set to the next smaller value such that the upper surface of ice transiently moves forward and stabilizes to an new shape, consistently with experiments (a) and (d) in Section 4.1. The position of the GL is recorded. This rule is repeated recursively until the lowest value of A_J . Then, the same procedure is run reversibly from the lowest value A_J to the highest one A_1 . For all value of the set of A_i , the experiment provides one position of the advancing GL and one for the retreating GL. Like Section 4.1, the ice sheet is considered to be in a steady state when the normalized annual volume change is lower than 10^{-6} .

To highlight the effects of the mesh and of the SIA additional component of the velocity, experiment (1a/2a) is run two times with an FG strategy of two various resolutions ($h \sim 7$ km and ~ 2 km) and the “SSA” model, once with an AG strategy and the “SSA” model and once with an AG strategy and the “SSA + SIA” model, see Section 3.2.3. In contrast, experiments (1b/2b), (3a), and (3b) are run with an AG strategy and the “SSA” model only. Adaptivity parameters are $h_{\min} \sim 0.1$ km, ~ 14 km and $L_f = 10$ km, i.e. the resolution close to the GL is ~ 100 m and ~ 10 km otherwise. In term of levels of refinement, this corresponds to $\underline{j} = 7$ and $\bar{j} = 14$, see Section 3.2.3.

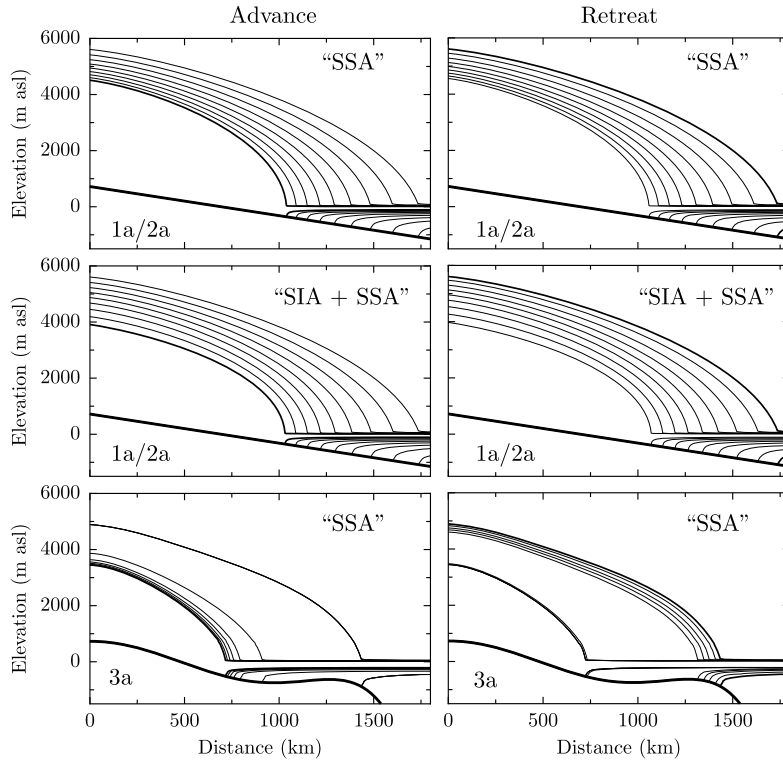


Fig. 4. Advancing (left) and retreating (right) steady state shapes for experiments (1a/2a) with SSA, (1a/2a) with “SSA + SIA” and (3a) with “SSA” when using an AG strategy. The bold line represents the steady state shape corresponding to the first parameter A (A_1 or A_J) while the other lines correspond to the other parameters A .

To validate our results, we use the following analytic expression for the ice softness parameter A with respect to the GL position x_{GL} :

$$A(x_{GL}) = [4^{p-1} C (a x_{GL})^{m+1}] / \left[(\rho g)^p \left(1 - \frac{\rho}{\rho_w} \right)^{p-1} \left(-\frac{\rho_w}{\rho} b(x_{GL}) \right)^{p+m+2} \right]. \quad (43)$$

This formula is derived from the boundary layer theory presented in [37] based on the SSA model, and is valid only for steady GLs.

Fig. 4 left (resp. right) displays the advancing (resp. retreating) steady state shapes reached when A is decreasing (resp. increasing) for experiments (1a/2a) (“SSA” and “SSA + SIA”) and (3a) (“SSA”) with an AG strategy. For both models, experiment (1a/2a) shows a regular advance of the GL for decreasing A and a quasi-symmetric retreat for re-increasing A . The reversibility of the GL is then verified in this case. As expected [37], this is no longer the case with experiment (3a) since a depression occurs in the bedrock. Indeed, when the advancing GL reaches the upward-sloping part of the bed, it jumps to the next downward-sloping part. The same appears during the retreating stage.

Fig. 5 displays the ice softness A as a function of the GL position for several grid strategies, models and experiments. Let us first focus on experiment (1a/2a) with the “SSA” model. For the lowest mesh resolution with FG strategy, the GL does not follow the advancing stages during retreating ones in a symmetric way. Indeed, when the parameter A re-increases, the GL remains stuck for a few stages before retreating. This delay was already observed in [43]. However, when using a finer mesh, the misfit between advancing and retreating positions decreases and the two phases get closer. Moreover, the GL positions converge to the analytic solution (43). The velocity field being less sharp for the lowest value of A , we observe that the GL position is better approximated for such value. For such values, the FG method with the finest resolution gets close to the analytic solution. Moreover, we observe (not shown) a linear convergence of the GL with respect to the mesh size, as observed in [8]. Interestingly, retreating GL positions are closer to the solution than advancing ones for low mesh resolutions. This is also slightly visible when using an AG strategy. This indicates that a finer mesh is required to represent the advancing GL than the retreating one with the same accuracy. As observed earlier, the GL is reversible and fits the analytic solution when strongly refining the mesh close to the GL. Consider now the entire “SSA + SIA” model. As a result, the steady state shapes are slightly thinner for the highest values of A and unchanged for the lowest compared to the ones obtained with the model “SSA”, see Fig. 4. This is the result of an increase of the ice flow due to the additional SIA component, which is negligible for the lowest values of A . We also observe that the positions of the GL fit the ones of the model “SSA” during the advancing stage, but show a slight delay of response during the retreating stage, see Fig. 5.

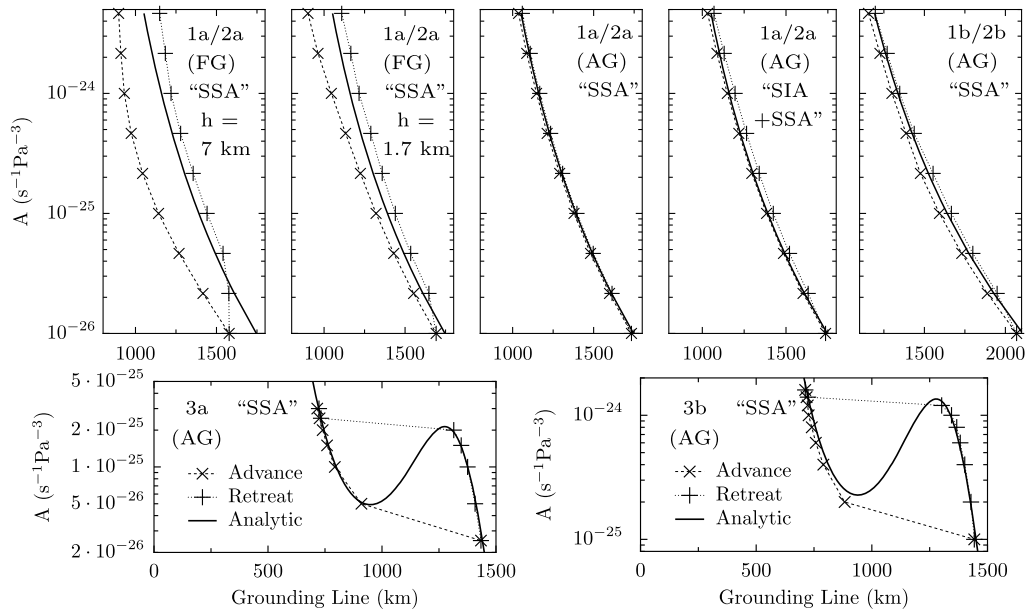


Fig. 5. Parameter A with respect to the GL position of the steady state shape for various MISIMIP 2D experiments, grid strategies and models. The analytic solution is drawn with the bold line from the formula (43).

As explained with further details in Section 4.3, this is a consequence of the diffusion step (step III), which rounds the surface between the ice sheet and the ice shelf and then moves forward the GL.

Let us now focus on experiment (1b/2b), which is slightly less reversible than the experiment (1a/2a). Indeed, the linear-type basal sliding parametrization induces a sharper and narrower transition in the SSA velocity, such that an even more intensive refinement is needed to improve the GL reversibility. Moreover, as already observed the retreating GL is closer to the solution than the advancing one. An additional experiment (not shown) with a greater accuracy close to the GL ($h_{\min} = 0.01$ km) shows indistinguishable advancing and retreating curves. As expected, the GL of experiment (3a) displays a jump where the bed is upward-sloping and the retreating stage takes a different path. Both advancing and retreating positions fit perfectly the analytic solution (43). Like experiment (1b/2b) compared to (1a/2a), the GL of experiment (3b) does not follow the analytic solution (43) as neatly as experiment (3a) does, especially during the advancing stages. However, the misfit in experiment (3b) can be reduced by further refining (to $h_{\min} = 0.01$ km) in this transition zone as done for experiment (1b/2b).

4.3. MISIMIP 3D

Two-dimensional ice sheets miss blustering effects on the Grounding Line (GL) that are induced by lateral stresses [15]. In order to capture these effects one has to include the second horizontal dimension. In this section, we report one of the MISIMIP 3D [33] experiments that involves a three-dimensional ice sheet. In contrast to MISIMIP 2D, MISIMIP 3D aims to verify the reversibility of the GL under a perturbation in the sliding parametrization C.

Consider the horizontal domain $\Omega = [0, 800] \times [0, 50]$ km and a flat sloppy bedrock defined by $b(x, y) = -100 - x/1000$, see Fig. 6. We assume a constant accumulation rate $a = 0.5$ m a⁻¹, such that the presence of an upstream ice sheet and of a downstream ice shelf are guaranteed. Symmetry is imposed at $x = 0$ km and at $y = 0$ km while, at the ocean boundary of the ice shelf ($x = 800$ km), the ice pressure is balanced by the hydrostatic sea water pressure (condition (17)). A free-slip boundary condition for the SSA (Eqs. (14) and (15)) occurs on the lateral side $y = 50$ km. As ice softness, we use the parameter $A = 10^{-25}$ Pa⁻³ s⁻¹, and as sliding law, we use $m = 1/3$ and

$$C(x, y) = \bar{C} \left[1 - \bar{a} \exp \left(-\frac{(x - \bar{x})^2}{2(150 \times 10^3)^2} - \frac{y^2}{2(10 \times 10^3)^2} \right) \right], \quad (44)$$

where \bar{x} is a given fixed x -coordinate, $\bar{a} \geq 0$ is the perturbation amplitude and $\bar{C} = 10^7$ Pa m^{-1/3} s^{1/3} [33]. When $\bar{a} = 0$, $C = \bar{C}$ is constant. When $\bar{a} > 0$, the sliding coefficient $C(x, y)$ contains a perturbation by a Gaussian function which is maximal at point $(\bar{x}_{GL,0}, 0)$ of the GL (black point in Fig. 6).

The MISIMIP 3D experiment consists of three steps, the model being transiently run with changing sliding conditions in (44). Like for MISIMIP 2D, the ice geometry of step 1 is initialized by a ten-meter-thick layer of ice (grounded and floating) on Ω . Afterwards, the initial geometries of steps 2 and 3 are taken from the last geometries obtained in steps 1 and 2, respectively. Steps 1, 2 and 3 are defined as follows.

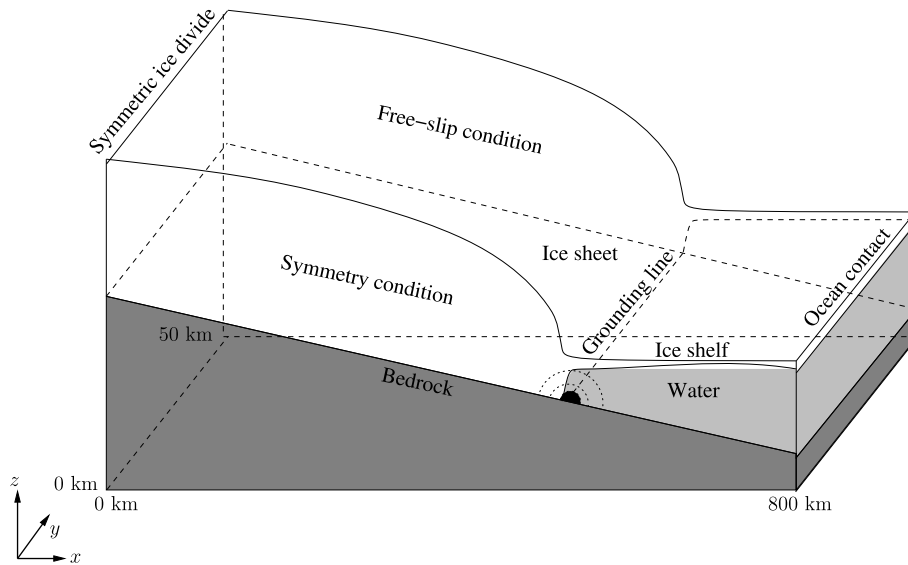


Fig. 6. Set-up of the MISIMP 3D experiment. The black point corresponds to the place where the perturbation is maximal.

Step 1: No perturbation is applied in the sliding condition (44), i.e. $\bar{a} = 0$.

The model is run until a steady state shape is reached.

Step 2: A perturbation is applied in (44) by setting $\bar{a} = 0.75$ and \bar{x} to the x -coordinate of the GL at the ordinate 0 and at the final time of step 1.

The model is run for 100 years.

Step 3: The perturbation is removed by setting $\bar{a} = 0$ in (44).

The model is run until a steady state shape is reached.

The ice sheet is considered to be in a steady state when the normalized annual volume change is lower than 10^{-6} , when the annual GL position change on side $x = 0$ km is lower than 1 m, and after a safe period of 10 000 years.

This MISIMP 3D experiment is run twice with the two different models “SSA” and “SSA + SIA”, such that the effects of the SIA component can be analyzed. For both models, we use the AG strategy only since the FG one already proved to be unable to reproduce the reversibility of the GL [33] with a reasonable number of mesh nodes. The corresponding parameter are $h_{\min} \sim 0.4$ km, ~ 6 km and $L_f = 20$ km, i.e. the resolution close to the GL is 400 meters and 6 km elsewhere. In term of levels of refinement, this corresponds to $j = 3$ and $\bar{j} = 7$, see Section 3.2.3. The GL positions and the horizontal surface velocity perpendicular to the GL at the end of Steps 1, 2 and 3 are displayed in Fig. 7 for both models. The evolution of the GL on the sides $x = 0$ km and $x = 50$ km during the first 100 years of step 2 and 3 are displayed in Fig. 8. Finally, an example of the mesh around the GL is shown in Fig. 9.

When using the “SSA” model, the GL position stabilizes at ~ 602 km uniformly in y (Fig. 7 top-left) at the end of step 1. Since the problem during step 1 is symmetric (without perturbation), no variation in y is expected. Moreover, we can compare this position to the analytic solution given by (43), which gives ~ 607 km. This discrepancy of 5 km is reasonable (and comparable to the accuracy obtained for MISIMP 2D) given the mesh size close to the GL: $h_{\min} \sim 0.4$ km. At the end of step 1, the velocity of the ice at the GL is nearly constant in y and about 400 m/a (Fig. 7 top-right). During step 2, the sliding perturbation lowers the friction on the side $y = 0$ km, which increases substantially the velocities, as seen in Fig. 7 top-right. Indeed, the velocity along the GL is nearly 1000 m/a on the perturbation side and 500 m/a on the other side. One hundred years later, the perturbed ice flow has moved forward the GL by ~ 11 km on side $y = 0$ km and moved backward the GL by ~ 7 km on side $y = 50$ km. Once the perturbation is removed (in step 3), the GL recovers its original position before perturbation with a high accuracy; both GLs are even indistinguishable in Fig. 7. This shows that the model “SSA” with an AG strategy allows us to reproduce a correct reversible GL.

Regarding the other model results in [33] we observe that, the deformation of GL under perturbation of ~ 20 km between both sides is comparable to most of the models, including those that are based on higher order mechanics, like TAL2, HGU2, DMA6, DPO1, RHI1, HSE1, RHI2, SCO4, SCO6, LFA1 [33]. Fig. 8 allows us to compare the evolution of the GL during steps 2 and 3 on both sides against the ones of the other models displayed in Fig. 6 in [33]. Disregarding some shifts in the position of the GL along the x -abscissa due to differences in mesh size, the evolution of our GL fits well the ones obtained with a similar model, i.e. based on the SSA and using an AG strategy like HGU1, DMA6, DGO1, RHI1 or RHI2. In particular, a common feature to all these models and ours is that step 1 does not show a monotonous transient advance of the GL on the perturbation side, but instead, a fast advance during the first 25 years, followed by a slow retreat the last 75 years. Such a behavior does not occur with the other models. Let us notice that the five cited models and ours all show a sym-

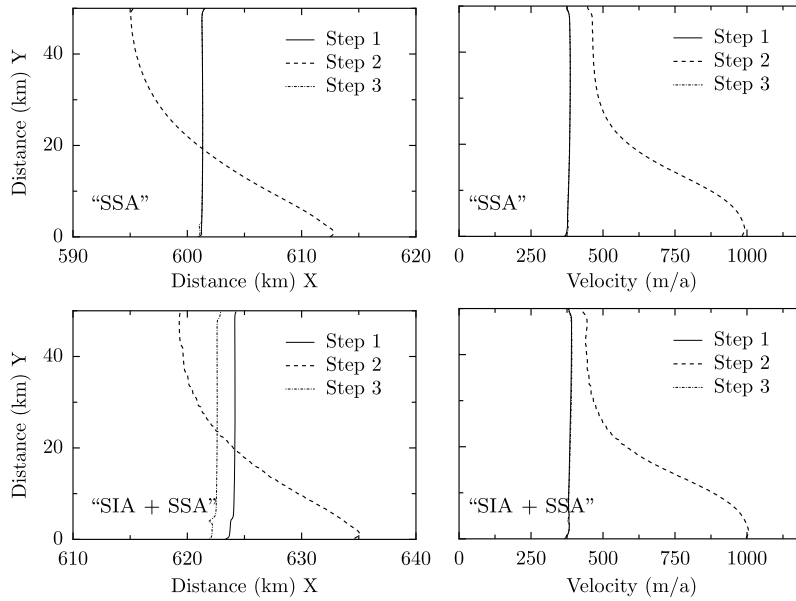


Fig. 7. Left: Sky-view of the GLs at the end of steps 1, 2 and 3 similarly to Fig. 5 in [33]. Right: horizontal surface velocity (SSA component only) perpendicular to the GL at the end of steps 1, 2 and 3 similarly to Fig. 4 in [33]. The results are given for both models “SSA” (top) and “SSA + SIA” (bottom). The x-axis of the left graphs are shifted by 20 km to facilitate comparison.

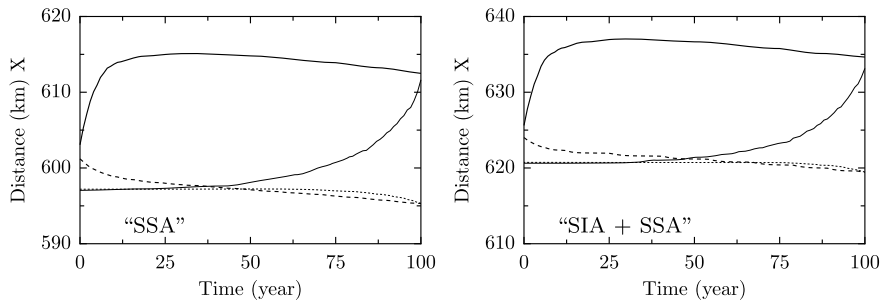


Fig. 8. Evolution of the GL on the side $x = 0$ km (continuous line) and the side $x = 50$ km (dashed line) during the 100 years of step 2 (bold line) and the first 100 years of step 3 (the time is reversed) similarly to Fig. 6 in [33]. Like in Fig. 7, the y-axis of the graphs are shifted by 20 km to facilitate comparison.

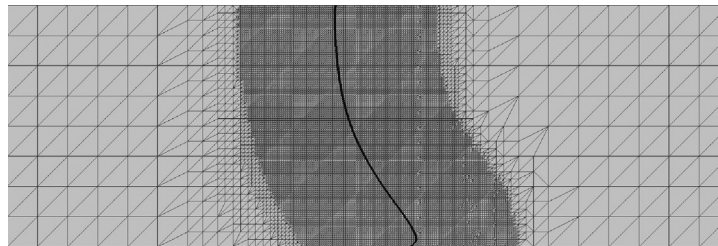


Fig. 9. Example of adaptive mesh at the end of the step 2. The mesh size close to the GL is ~ 400 m and 6 km elsewhere.

metric GL (no variation in y) after 100 years of the step 3, but require longer to recover to the position they had before the perturbation.

Using the model “SSA + SIA” instead of “SSA” shows some differences in term of the GL position, see Figs. 7 and 8. First, the GL is shifted downstream by about 24 km at the end of step 1. Then, even shifted, the GL deforms very similarly to the “SSA” case during step 2. Finally, the GL almost recovers its position before perturbation, however ~ 2 km upstream. As observed with experiment (1a/2a) of MISMIP 2D, adding the SIA component of the velocity makes the modeled GL slightly less reversible after being perturbed. Most importantly, the GL stabilizes farther downstream with the SIA than without, while one should have expected the opposite. Indeed, including the SIA component should result in faster flow, a smaller ice cap and a GL position farther upstream [33]. All higher order models of [33] confirms such sense of the deviation

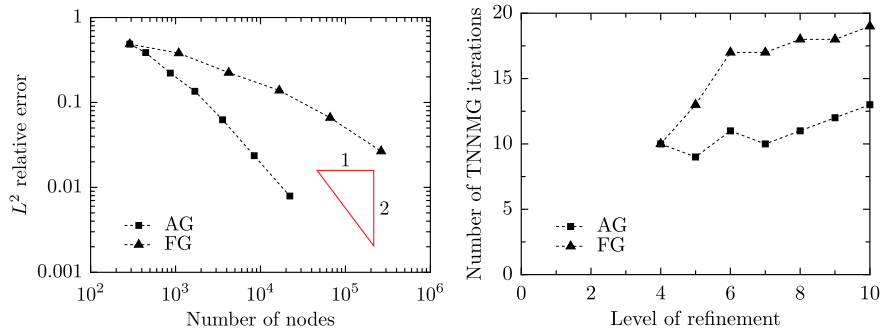


Fig. 10. Left: L^2 relative error with respect to the number of mesh nodes. Right: Number of TNNMG iterations to reach convergence with respect to the level of refinement.

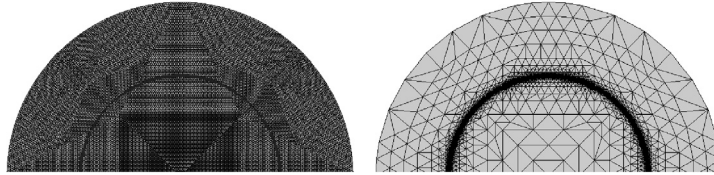


Fig. 11. FG (left) and AG (right) mesh of the half upper part of the disk Ω . On the left, the GL is materialized by a thick black line, while, on the right, the GL is covered by an intensive refinement.

between differently modeled GLs, including the Schoof–Hindmarsh model [8], but except the only other superposed “SSA + SIA” (compare TAL1 and TAL2 in Fig. 5 of [33]). As a consequence, this artefact is specific to the superposed “SSA + SIA” model. It can be explained as follows. In contrast to other higher models, the “SSA + SIA” is entirely decoupled such that the vertical shearing does not reduce the effective viscosity in the SSA, like in the Schoof–Hindmarsh model. For instance, comparing Fig. 7 right-top and right-bottom show that the SSA velocities are almost unaffected by the additional SIA component. Instead of reducing the ice flow, the SSA component acts like a diffusion of the top surface, which transfers some mass downward making the ice sheet terminus more rounded and moving the GL forward.

4.4. Performance of the TNNMG method

We now evaluate the performances of the TNNMG method to compute a single SSA velocity field (step I) of a three dimensional ice sheet. To perform such a task, we define Ω as being the disk of radius 2000 km centred at the origin and consider the radial extension of the steady state shape of the experiment (1a/2a) in MISIP 2D obtained for the highest parameter A to define the ice sheet geometry (b , h , l and s). The goal of this section is to compare the convergence and the computational costs of the TNNMG algorithm for both meshing strategies, FG and AG.

For the sake of comparison, we first compute the solution on a uniform fine mesh, which is later considered as the exact solution. This mesh contains 10 levels of refinement, i.e. $(\underline{j}, \bar{j}) = (10, 10)$ and 1000000 nodes. Then, we perform the same computation on uniformly refined meshes (FG) $(\underline{j}, \bar{j}) = (j, j)$ for $j = 5, \dots, 9$ and adaptively refined meshes (AG) $(\underline{j}, \bar{j}) = (5, j)$ for $j = 5, \dots, 9$. For adaptive meshes, the parameter $L_f = 10$ km is chosen to provide an optimal ratio between the number of mesh nodes and the error. For both sequences of meshes, we compute the L^2 error (Fig. 10 left) and display the number of TNNMG iterations necessary to reach convergence with respect to the level of refinement j (Fig. 10 right). The finest AG and FG meshes are shown in Fig. 11.

Fig. 10 left indicates an improved convergence (close to be of order 2) of the AG approach compared to the FG approach to solve the SSA equation. In practice, the adaptive mesh $(\underline{j}, \bar{j}) = (5, 9)$ has only 8433 nodes while the mesh $(\underline{j}, \bar{j}) = (9, 9)$ has 263169 nodes (about 30 times more nodes) for the same accuracy of the solution. However, the computational cost also depends on the number of TNNMG iterations that are necessary to reach convergence (when the global correction in the steps (28)–(32) is sufficiently small). Fig. 10 right indicates that such number of iterations remains approximatively constant when the mesh is locally or globally refined. As explained in Section 3.2.1, the effort spent in one TNNMG iteration is proportional to the number of mesh nodes. Thus also the overall CPU time is broadly proportional to this. For instance, it (on a single 3.30 GHz processor) was 4581 s and 99 s to solve the solution on the finest mesh (9, 9) and the adaptively refined mesh (5, 9), respectively.

Let us mention that, in practise, one single iteration of the TNNMG method is performed for the SSA (step I) and one for the SIA (step III) at each time step when solving the time-dependent problem. Indeed, further iterations are not needed since the time steps, which are constrained by a CFL condition, are small (in the MISIP experiments, the time steps range between 0.1 and 0.5 years). In addition, we noticed that computing the SIA (step III) is ~ 5 times computationally cheaper compared to computing the SSA (step I). For instance, in the experiment (1a/2a) of MISIP 2D using the “SSA + SIA”

model and the AG strategy, step I and step III require ~ 0.05 and ~ 0.01 s, the mesh containing ~ 330 nodes in average. Finally, it takes about 35 h to compute the $\sim 1\,000\,000$ time steps needed to obtain the 18 steady shapes. In the MIS-MIP 3D experiment using the “SSA + SIA” model, step I and step III require about 6 and 1 s to be solved, the mesh containing $\sim 15\,000$ nodes in average. The overall experiment takes about 60 hours to compute the $\sim 25\,000$ time steps.

5. Conclusions and perspectives

In this paper, we implemented a new Newton multigrid method to solve the SSA equation and the diffusive part of the mass conservation equation, which derives from the SIA. Numerical results have demonstrated the mesh-independent convergence of our method, making the implementation of an adaptive mesh refinement procedure relevant. On one example, our heuristic adaptive strategy proved to be second order convergent. Our results were validated against an exact solution (MISMIP 2D) and against other model results (MISMIP 3D).

In all MISMIP experiments, adaptivity was found essential to reproduce the correct motion of the GL with reasonable computational cost. Using the reversibility of the GL as a criterion to assess the quality of the mesh, we found that ~ 100 -m-large elements were needed in a ~ 20 -km-large zone surrounding the GL zone, while ~ 10 -km-large elements were enough outside this zone. Such numbers were found empirically and are expected to change when using different parameters. Ideally, an adaptive procedure should be independent of any physical parameter. In particular, implementing residual or hierarchic *a posteriori* error estimators for the SSA equation, like the ones proposed in [2] and [45] respectively, might be one way to build more robust local refinement procedures. This issue will be addressed in a future work.

Our model was based on the linear superposition of a one-dimensional vertical model (SIA) and a two-dimensional horizontal model (SSA) to reconstruct the three-dimensional ice flow. Even if this superposition is physically justified for most of ice sheets and ice shelves [43], our model showed a wrong behavior of the GL in the MISMIP 3D experiment since the superposition “SSA + SIA” does not account for the SIA to compute the SSA effective viscosity. One way to recover such an anomaly would be to upgrade the model to the Schoof–Hindmarsh model like in [8].

Acknowledgements

The authors thank Ralf Kornhuber for his support, Ed Bueler for helpful discussions and Maria Baden for English proof-reading.

References

- [1] J.L. Bamber, W.P. Aspinall, An expert judgement assessment of future sea level rise from the ice sheets, *Nature Climate Change* 3 (2013) 424–427.
- [2] J. Baranger, H. El Amri, Estimateurs *a posteriori* d'erreur pour le calcul adaptatif d'écoulements quasi-newtoniens, *RAIRO – Modélisation Mathématique et Analyse Numérique* 25 (1991) 31–47.
- [3] J.W. Barrett, W.B. Liu, Finite element approximation of the p -Laplacian, *Mathematics of Computation* 61 (1993) 523–537.
- [4] R. Bermejo, J.A. Infante, A multigrid algorithm for the p -Laplacian, *SIAM Journal on Scientific Computing* 21 (December 1999) 1774–1789.
- [5] H. Blatter, Velocity and stress fields in grounded glaciers: A simple algorithm for including deviatoric stress gradients, *Journal of Glaciology* 41 (138) (1995) 333–344.
- [6] J. Brown, B. Smith, A. Ahmadi, Achieving textbook multigrid efficiency for hydrostatic ice sheet flow, *SIAM Journal on Scientific Computing* 35 (2) (2013) 359–375, <http://dx.doi.org/10.1137/110834512>.
- [7] E. Bueler, J. Brown, Shallow shelf approximation as a “sliding law” in a thermomechanically coupled ice sheet model, *Journal of Geophysical Research – Earth Surface* 114 (F3) (July 2009) F03008+.
- [8] S. Cornford, D.F. Martin, D.T. Graves, D.F. Ranken, A.M. Le Brocq, R.M. Gladstone, A.J. Payne, E.G. Ng, W.H. Lipscomb, Adaptive mesh, finite volume modeling of marine ice sheets, *Journal of Computational Physics* (2013) 529–549.
- [9] D. Docquier, L. Perichon, F. Pattyn, Representing grounding line dynamics in numerical ice sheet models: Recent advances and outlook, *Surveys in Geophysics* 32 (2011) 417–435.
- [10] G. Durand, O. Gagliardini, B. de Fleurian, T. Zwinger, E. Le Meur, Marine ice sheet dynamics: Hysteresis and neutral equilibrium, *Journal of Geophysical Research* 114 (2009).
- [11] G. Durand, O. Gagliardini, T. Zwinger, E. Le Meur, R.C.A. Hindmarsh, Full Stokes modeling of marine ice sheets: Influence of the grid size, *Annals of Glaciology* 50 (52) (2009) 109–114.
- [12] D.L. Egholm, S.B. Nielsen, An adaptive finite volume solver for ice sheets and glaciers, *Journal of Geophysical Research* 115 (2010) F01006.
- [13] A. Ern, J.L. Guermond, *Theory and Practice of Finite Elements*, Springer, 2004.
- [14] R. Glowinski, *Handbook of Numerical Analysis: Numerical Methods for Fluids (Part 3)*, vol. 9, Elsevier Science Ltd, 2003.
- [15] D. Goldberg, D.M. Holland, C. Schoof, Grounding line movement and ice shelf buttressing in marine ice sheets, *Journal of Geophysical Research* 114 (F04026) (2009).
- [16] C. Gräser, *Convex minimization and phase field models*, PhD thesis, FU, Berlin, 2011.
- [17] C. Gräser, R. Kornhuber, Multigrid methods for obstacle problems, *Journal of Computational Mathematics* 27 (1) (2009) 1–44.
- [18] C. Gräser, U. Sack, O. Sander, Truncated nonsmooth Newton multigrid methods for convex minimization problems, in: *Domain Decomposition Methods in Science and Engineering XVIII*, in: *Lecture Notes in Computational Science and Engineering*, vol. 70, Springer, Berlin, Heidelberg, 2009, pp. 129–136.
- [19] C. Gräser, O. Sander, The dune-subgrid module and some applications, *Computing* 86 (4) (2009) 269–290.
- [20] C. Gräser, O. Sander, Polyhedral Gauß–Seidel converges, *Matheon*, 2010, Preprint 696.
- [21] R. Greve, H. Blatter, *Dynamics of Ice Sheets and Glaciers*, Springer-Verlag, 2009.
- [22] W. Hackbusch, *Multi-Grid Methods and Applications*, Springer Series in Computational Mathematics, Springer, 1985.
- [23] Y.Q. Huang, R. Li, W. Liu, Preconditioned descent algorithms for p -Laplacian, *Journal of Scientific Computing* 32 (August 2007) 343–371.
- [24] I. Joughin, R.B. Alley, Stability of the west antarctic ice sheet in a warming world, *Nature Geoscience* 4 (2011) 506–513.
- [25] G. Jouvét, E. Bueler, Steady, shallow ice sheets as obstacle problems: Well-posedness and finite element approximation, *SIAM Journal on Applied Mathematics* 72 (4) (2012) 1292–1314.

- [26] G. Jouvét, E. Bueler, C. Gräser, R. Kornhuber, A nonsmooth Newton multigrid method for a hybrid, shallow model of marine ice sheets, 8th International Conference on Scientific Computing and Applications, AMS, 2012.
- [27] R. Kornhuber, Monotone multigrid methods for elliptic variational inequalities. I, *Numerische Mathematik* 69 (2) (1994) 167–184.
- [28] R. Kornhuber, Nonlinear multigrid techniques, in: *Theory and Numerics of Differential Equations*, Springer, 2001, pp. 179–229.
- [29] E.Y. Larour, H. Seroussi, M. Morlighem, E. Rignot, Continental scale, high order, high spatial resolution, ice sheet modeling using the Ice Sheet System Model (ISSM), *Journal of Geophysical Research* 117 (2012).
- [30] R.J. Leveque, *Finite Volume Methods for Hyperbolic Problems*, Cambridge Univ. Press, 2002.
- [31] W.S.B. Paterson, *The Physics of Glaciers*, 3rd edition, Pergamon, 1994.
- [32] F. Pattyn, A. Huyghe, S. De Brabander, B. De Smedt, Role of transition zones in marine ice sheet dynamics, *Journal of Geophysical Research* 111 (F2) (2006) 1–10.
- [33] F. Pattyn, L. Perichon, G. Durand, L. Favier, O. Gagliardini, R.C.A. Hindmarsh, T. Zwinger, T. Albrecht, S. Cornford, D. Docquier, J.J. Furst, D. Goldberg, H. Gudmundsson, A. Humbert, M. Hutten, P. Huybrechts, G. Jouvét, T. Kleiner, E. Larour, D. Martin, M. Morlighem, A.J. Payne, D. Pollard, M. Ruckamp, O. Rybak, E. Seroussi, M. Thoma, N. Wilkens, Grounding-line migration in plan-view marine ice-sheet models: Results of the ice2sea MISIMP3d intercomparison, *Journal of Glaciology* 59 (215) (2013) 410–422, <http://dx.doi.org/10.3189/2013JoG12J129>.
- [34] F. Pattyn, C. Schoof, L. Perichon, R.C.A. Hindmarsh, E. Bueler, B. de Fleurian, G. Durand, O. Gagliardini, R. Gladstone, D. Goldberg, G.H. Gudmundsson, V. Lee, F.M. Nick, A.J. Payne, D. Pollard, O. Rybak, F. Saito, A. Vieli, Results of the Marine Ice Sheet Model Intercomparison Project, MISIMP, *The Cryosphere Discussions* 6 (1) (2012) 267–308.
- [35] C. Raymond, Deformation in the vicinity of divides, *Journal of Glaciology* 34 (1983) 357–373.
- [36] C. Schoof, Variational methods for glacier flow over plastic till, *Journal of Fluid Mechanics* 555 (2006) 299–320.
- [37] C. Schoof, Ice sheet grounding line dynamics: Steady states, stability, and hysteresis, *Journal of Geophysical Research* 112 (F3) (July 2007) F03S28+.
- [38] C. Schoof, Coulomb friction and other sliding laws in a higher order glacier flow model, *Mathematical Models and Methods in Applied Sciences* (2009).
- [39] H. Séroussi, Modeling ice flow dynamics with advanced multi-model formulations, PhD thesis, Ecole Centrale Paris, 2011.
- [40] J. Stoer, R. Bulirsch, *Introduction to Numerical Analysis*, 3rd edition, Springer, Berlin, New York, 2002.
- [41] I. Velicogna, J. Wahr, Measurements of time-variable gravity show mass loss in Antarctica, *Science* 311 (5768) (2006) 1754–1756.
- [42] A. Vieli, A.J. Payne, Assessing the ability of numerical ice sheet models to simulate grounding line migration, *Journal of Geophysical Research* 110 (F1) (2005) 1–18.
- [43] R. Winkelmann, M.A. Martin, M. Haseloff, T. Albrecht, E. Bueler, C. Khroulev, A. Levermann, The potsdam parallel ice sheet model (PISM-PIK) Part 1: Model description, *The Cryosphere* 5 (2011) 715–726.
- [44] J. Xu, The method of subspace corrections, in: *Numerical Analysis 2000*, vol. VII, Partial Differential Equations, in: *Journal of Computational and Applied Mathematics*, vol. 128 (1–2), 2001, pp. 335–362.
- [45] Q. Zou, A. Veiser, R. Kornhuber, C. Gräser, Hierarchical error estimates for the energy functional in obstacle problems, *Numerische Mathematik* 117 (2011) 653–677.